

3D Imaging of Atom Clouds from 2D Projections

Murtaza Safdari
Stanford University
Stanford CA 94305
murtazas@stanford.edu

Abstract

Mid band gravity detectors such as the MAGIS[1] experiment rely on the imaging of the interfering atoms as they fluoresce from the excitation imparted by the driving laser. This project presents a novel opportunity to develop an imaging system that capture details of the 3D shape of the clouds at different points along the beam line. Advantage of using telecentric lenses is also probed for such imaging systems.

1. Introduction

Atom interferometry experiments such as MAGIS [1] promise to open up an explored band of gravity wave signals to detections. A key part of these experiments is the ability to monitor the atom clouds that interfere in the arms of the experiments. Conventional imaging systems used for these purposes rely on simple entocentric systems that are sufficient to acquire the location of the cloud within the field of view of the imaging system. This opens up the possibility of deploying advanced systems that can not only monitor the position of the atom clouds, but also give information about the 3D shape of these clouds being driven in these experiments.

In this work we will explore the possibility of reconstructing the 3D details of the atom clouds from 2D images acquired by imaging systems that capture three orthogonal views of the atom clouds. We will also explore the possibility of using telecentric lenses in such systems and study the desirable properties of telecentric versus entocentric lenses.

This report is structured as follows: In **Section 2** we'll dive into the advantages of telecentric systems and develop the models for telecentric and entocentric images to be used in the reconstruction. In **Section 3** the 3D reconstruction techniques used are described, and in **Section 4** we compare the results for various techniques and cloud geometries. Finally, we summarize the results, discuss future work and limitations in **Section 5**.

2. Imaging Models

Under the assumption that the atom clouds are non-occluding, that is 2D projections are line integrals, we can develop the following models.

2.1. Entocentric Systems

These systems can be well described by the pinhole camera model. For the purposes of this project, we are concerned with how the 3D clouds map to their 2D projections in entocentric imaging systems. The key point here is that the magnification of entocentric systems changes as the object distance changes.

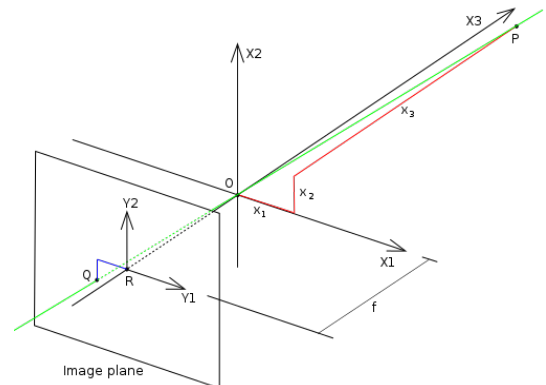


Figure 1 An image showing the mapping from 3D to 2D by a pinhole camera [2]

From **Figure 1** we can deduce that the scale of the mapping from $X1 \rightarrow Y1$ and $X2 \rightarrow Y2$ depends on the distance ratio $f/x3$ along the optical axis of the pinhole. The magnification is, $m = f/x3$.

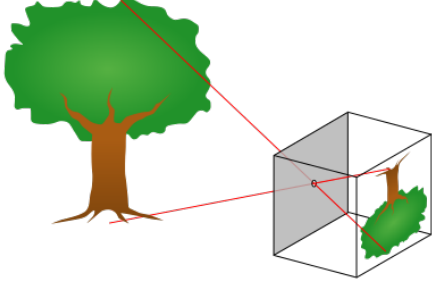


Figure 2 Effect of magnification on light collected [3]

From **Figure 2** we can see that the magnification also plays a role in how much light is collected from an object at a given depth. Assuming we have a surface of area A at some distance d_1 corresponding to magnification m_1 from the pinhole, or at another distance corresponding to magnification m_2 , we see that the light density collected at the sensor is the same in both cases,

$$\frac{I\alpha^2}{m_1^2 A} = \frac{I\alpha^2 m_2^2}{m_2^2 A}$$

Where $\alpha \sim \tan^{-1}(\sqrt{A}/d_1)$, I is the light intensity emitted from the object per solid angle steradian, and in the small angle approximation, $(1 - \cos \alpha) \sim \alpha^2$.

Therefore, the entocentric 2D projections of the 3D clouds can be made by slicing the 3D object in planes perpendicular to the axis of projection, resizing them with simple linear interpolation to the appropriate scale, and adding them up.

2.2. Telecentric Systems

We will restrict ourselves to bi-telecentric systems for this work. These systems have the capability to capture images of objects at different depths with the same magnification, which greatly simplifies the 2D projection process. This is highlighted in **Figure 3**.

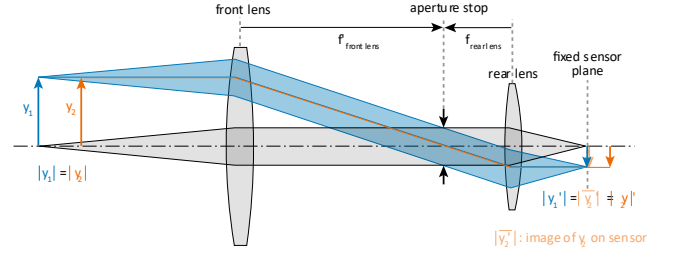


Figure 3 A system made double telecentric with a stop placed in the back (front) focal plane of the first (second) lens [4]

The equal magnification also ensures that the angular aperture of pencil beams emanating from points at different depths is equal [5].

Therefore, the telecentric 2D projections of the 3D clouds can be made by slicing the 3D object in planes perpendicular to the axis of projection, and simply adding them up linearly.

3. 3D Reconstruction technique

The reconstruction from 2D projections to the 3D cloud is an inverse problem in compressive sensing [6]; We are solving the set of equations $\mathbf{A}(x) = b$, for the 3D cloud x given the 2D projections b . Being underdetermined, we rely on priors to guide us to the x solution.

We converge to a solution of x by minimizing the residual,

$$R = \frac{1}{2} \|\mathbf{A}(x) - b\|_2^2 + \lambda \Gamma(x)$$

here $\Gamma(x)$ is the guiding prior, and λ is a hyper-parameter. The choice of prior will be informed by the physics of the atom clouds, hence we consider 2 canonical cloud topographies:

1. Uniform density atom clouds; any unit volume in space is either filled with some fixed density or is null.
2. Smoothly varying density clouds; the density varies smoothly across volume.

The corresponding priors are therefore:

1. $\Gamma(x) = \|\mathbf{D}^1(x)\|_2^1$ for uniform density clouds; we want sparse gradients
2. $\Gamma(x) = \|\mathbf{D}^2(x)\|_2^2$ or $\|\mathbf{D}^2(x)\|_2^1$ for smoothly dense clouds; we want slowly varying densities in space

In the case of $\Gamma(x)$ that is an L2 Norm, we can find the extrema of the residual analytically, and use conjugate gradients to perform the inversion,

$$R = \frac{1}{2} \|\mathbf{A}(x) - b\|_2^2 + \lambda \|\mathbf{D}^2(x)\|_2^2$$

$$R' = 0 \rightarrow x = \left(\mathbf{A}^T \mathbf{A} + \lambda \mathbf{D}^{2T} \mathbf{D}^2 \right)^{-1} \mathbf{A}^T(b)$$

For $\Gamma(x)$ that are L1 Norms, we can use ADMM [7] to iteratively converge to the optimal solution. Block soft thresholding [8] is used to tackle the update step for the L1 norm penalty operator. We show below the update steps,

$$\text{minimize}_{\{x\}} \frac{1}{2} \|\mathbf{A}(x) - b\|_2^2 + \lambda \Gamma(z)$$

$$\text{subject to } \mathbf{K}x - z = 0$$

The Augmented Lagrangian L ,

$$L = \frac{1}{2} \|\mathbf{A}(x) - b\|_2^2 + \lambda \Gamma(z) + y^T (\mathbf{K}x - z) + \frac{\rho}{2} \|\mathbf{K}x - z\|_2^2$$

Every iteration,

$$x \leftarrow (\mathbf{A}^T \mathbf{A} + \rho \mathbf{K}^T \mathbf{K})^{-1} (\mathbf{A}^T(b) + \rho \mathbf{K}^T(z - u))$$

$$z \leftarrow \left(1 - \frac{\lambda/\rho}{\|\mathbf{K}x + u\|_2} \right) (\mathbf{K}x + u)$$

$$u \leftarrow u + \mathbf{K}x - z$$

For $u = (1/\rho)y$. \mathbf{K} is the L1 Norm penalty operator $\|\mathbf{D}^1(x)\|_2^1$ or $\|\mathbf{D}^2(x)\|_2^1$.

We set the parameters $\lambda = 1$ and $\rho = 10$ throughout this project as this represents a good working point for both the inversion methods listed above.

Computational speedups can be harvested by restricted the volume over which the inversion process occurs. To this end, Visual Hulls [9] were seen as a possible avenue for gain, and we extract the visual hulls from the 2D projections for this purpose.

4. Analysis Results & Evaluation

4.1. Canonical Atom Clouds

As mentioned in the previous section, we consider two canonical cloud topographies:

1. Uniform density atom clouds
2. Smoothly varying density clouds

Following are the shapes of these typical clouds used to test the 3D reconstruction technique.

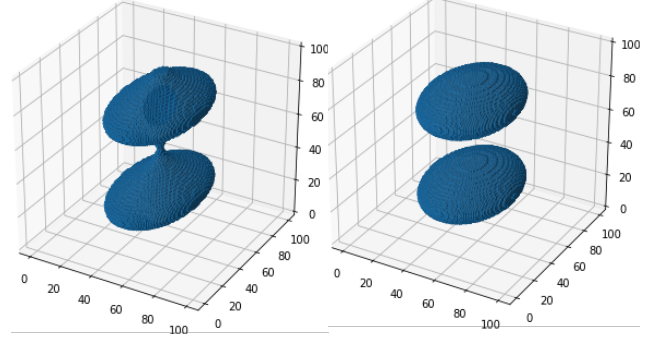


Figure 4 Shapes of canonical clouds; (Left) Uniform density cloud with cavity in upper lobe; (right) Smooth density cloud

From **Figure 4** we can see the structure of the typical clouds we are considering; These are made of two bulbs with some separation. We have introduced a concavity to the uniform density cloud in the form of a cavity hidden within the mass of the upper lobe. Whereas in the case of the smooth cloud we have concavity by virtue of the variable density.

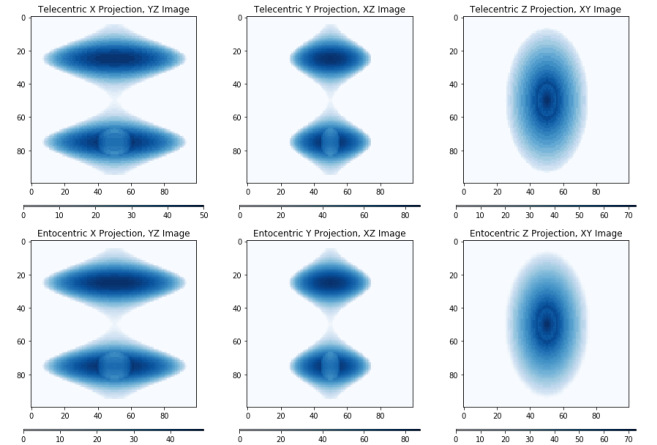


Figure 5 Telecentric (top) and Entocentric (bottom) inverted 2D projections along the X, Y, Z axes for Uniform Density Cloud

In **Figure 5** we can see the 2D projections that result from the uniform density cloud. Note the effect of the cavity in the lobes. These serve as the input images that the reconstruction will see for the case of the uniform density cloud. In **Figure 6** we can see the very same for the case of the smoothly varying density cloud.

We can see from these figures that the difference between telecentric and entocentric projections is a subtle blurring in the entocentric case.

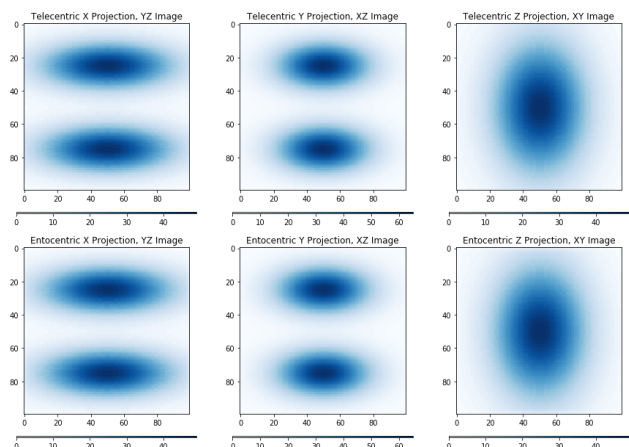
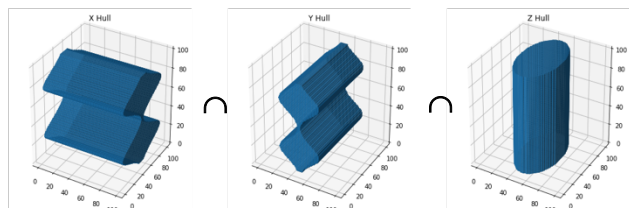


Figure 6 Telecentric (top) and Entocentric (bottom) inverted 2D projections along the X, Y, Z axes for Smooth Density Cloud

4.2. Visual Hulls

Using the 2D projections for each cloud, we perform a simple visual hull extraction by taking the intersection of the hull generated using each projection. This is illustrated explicitly for the telecentric case of the uniform cloud below.



We can repeat this procedure for telecentric and entocentric projections from the 2 clouds, which result in the following hulls.

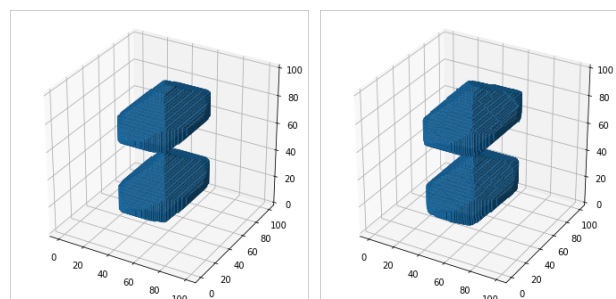


Figure 7 (left) Telecentric, (right) Entocentric Visual Hull for Uniform Density Cloud

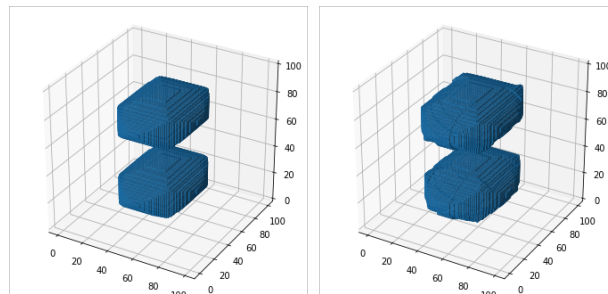


Figure 8 (left) Telecentric, (right) Entocentric Visual Hull for Smoothly Varying Density Cloud

We note here that in the case of the uniform density cloud, the body of the hull is filled with compatible voxel values. However, in the case of smoothly varying density, the hull is filled with the maximum voxel density allowed, which necessarily overestimates the true voxel values.

4.3. Qualitative 3D Reconstruction Results

We now present the best results for the various projections for the two clouds.

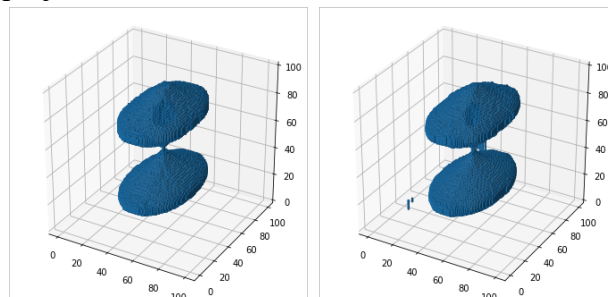


Figure 9 (left) Telecentric, (right) Entocentric 3D Reconstructed Cloud for the Uniform Density Case

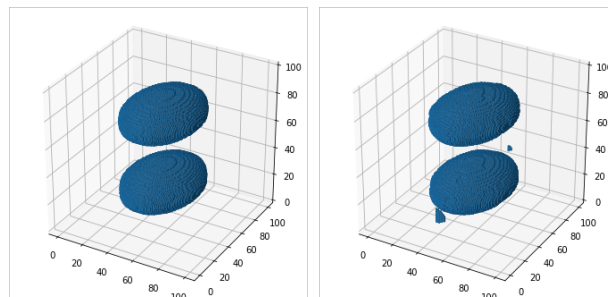


Figure 10 (left) Telecentric, (right) Entocentric 3D Reconstructed Cloud for the Smoothly Varying Density Case, using the $\|D^2(x)\|_2^1$ prior.

From the above figures, we can conclude that the 3D reconstruction does a good job of recovering the structure of the true atom clouds,

	Uniform Density Cloud		Smoothly Varying Density Cloud		
<u>telecentric</u> <u>entocentric</u>	$\ \mathcal{D}^1(\mathbf{x})\ _2^1$	Visual Hull Only	$\ \mathcal{D}^2(\mathbf{x})\ _2^1$	$\ \mathcal{D}^2(\mathbf{x})\ _2^2$	Visual Hull Only
PSNR	25.95/20.90	16.96/11.76	33.89/32.08	29.21/8.956	18.69/12.49
Recon Err	.0686/.1314	.1700/.5639	.0246/.0361	.0769/2.523	.1146/.4780

Table 1 PSNR and Recon Err values for the various projections, priors used for the clouds.

even recovering the concavities in both cases. We note that telecentric projections produce a slightly higher fidelity 3D clouds than entocentric ones.

4.4. Quantitative 3D Reconstruction Results

To derive quantitative results on the reconstructed clouds, we use two figures of merit: Peak Signal to Noise Ratio, and Reconstruction Error.

$$\text{PSNR} = 10 \log_{10}(1/\|voxel_{reco} - voxel_{true}\|^2)$$

$$\text{Recon Err} = \sum \|voxel_{reco} - voxel_{true}\|^1 / \sum voxel_{true}$$

Recon Err is designed to encapsulate the expected per voxel density error within the 3D cloud. The numerical results are compiled in **Table 1**.

Note that it is not possible to compare the numbers from one cloud to the other directly as we have binary numbers in the uniform cloud and floating-point numbers in the smooth cloud.

4.5. Observations

We can compare the results of 3D reconstruction to visual hull extraction. 3D reconstruction does a better job as expected. This is especially true for the smoothly varying density cloud where the visual hull overestimates the voxels.

Furthermore, performance of 3D reconstruction is better with telecentric projections than entocentric projections. This makes sense as the entocentric projections are complicated by the magnification. Therefore, convergence to the optimal solution is expected to be more difficult.

We observe that using $\|\mathcal{D}^2(\mathbf{x})\|_2^1$ produces higher fidelity 3D clouds than $\|\mathcal{D}^2(\mathbf{x})\|_2^2$. This may be an artifact of the reconstruction used; ADMM convergence is likely better than the simple CG inversion for the set of parameters tested. The physics of the cloud does not necessarily prefer sparsifying $\|\mathcal{D}^2(\mathbf{x})\|_2$ versus making it small.

Finally, we note that convergence failed for the smoothly varying density cloud when using the L2 norm (low PSNR and high Recon Err).

5. Conclusions

In this project we set out to investigate the viability of utilizing just three 2D views of atom clouds for the purposes of 3D reconstruction. The project has demonstrated that this is entirely feasible in simulations under realistic assumptions about the atom clouds. This presents an exciting opportunity to introduce a new way of visualizing the 3D details of interfering atom clouds. Furthermore, we have shown that the 3D reconstruction technique is able to recover concavities, paving the way for performing measurements previously inaccessible from the 2D views of the atom clouds.

We also considered the benefits of using telecentric imaging systems and found that there is an improvement in fidelity when using such systems. However, a detailed study about the light loss in these lenses, along with a more in-depth study of the performance of telecentric versus entocentric systems for 3D reconstruction, is needed for before any recommendations can be made either way.

References

- [1] P. Graham, J. Hogan, M. Kasevich, S. Rajendran, “New method for gravitational wave detection with atomic sensors.,” PRL, 110, 17, Apr. 2013.
- [2] Creative Commons Image,
<https://en.wikipedia.org/wiki/File:Pinhole.svg>
- [3] Creative Commons Image,
<https://commons.wikimedia.org/wiki/File:Pinhole-camera.svg>
- [4] Protected Use Image,
https://www.silloptics.de/fileadmin/user_upload/Bilder%20Homepage/Bitelezentrische%20Objektive_EN.svgA.
- [5] K. Lenhardt and B. Kreuznach, “Optical measurement techniques with telecentric lenses,” Schneider Kreuznach.
<https://schneiderkreuznach.com/application/files/9715/0781/8897/optical-measurement.pdf>
- [6] Wakin, M., Laska, J., Duarte, M., Baron, D., Sarvotham, S., Takhar, D., Kelly, K., & Baraniuk, R. 2006. An architecture for compressive imaging. In Proc. International Conference on Image Processing (ICIP).
- [7] Boyd, S., Parikh, N., Chu, E., Peleato, B., AND Eckstein, J. 2001. Distributed optimization and statistical learning via the alternating direction method of multipliers. Foundations and Trends in Machine Learning 3, 1, 1–122.
- [8] Rudin, L., Osher, S., & Fatemi, E. 1992. Nonlinear total variation based noise removal algorithms. Physica D: Nonlinear Phenomena 60, 14, 259 – 268.
- [9] A. Laurentini, “The visual hull concept for silhouette-based image understanding,” IEEE Transactions on Pattern Analysis and Machine Intelligence, vol. 16, no. 2, Feb. 1994.